A TRIDENT SCHOLAR PROJECT REPORT

NO. 532

Experimental Determination of Energy Absorption Characteristics of a Cylindrical Wave Energy Converter in Linear and Nonlinear Waves

by

Midshipman 1/C Ryan M. Conway, USN

UNITED STATES NAVAL ACADEMY
ANNAPOLIS, MARYLAND

USNA-1531-2

REPORT DOCUMENTATION PAGE

Form Approved
OMB No. 0704-0188

1. REPORT DATE *(DD-MM-YYYY)*	**2. REPORT TYPE**	**3. DATES COVERED** *(From - To)*
5-16-23		

4. TITLE AND SUBTITLE

Experimental Determination of Energy Absorption Characteristics of a Cylindrical Wave Energy Converter in Linear and Nonlinear Waves

5a. CONTRACT NUMBER

5b. GRANT NUMBER

5c. PROGRAM ELEMENT NUMBER

6. AUTHOR(S)

Ryan M. Conway

5d. PROJECT NUMBER

5e. TASK NUMBER

5f. WORK UNIT NUMBER

7. PERFORMING ORGANIZATION NAME(S) AND ADDRESS(ES)

8. PERFORMING ORGANIZATION REPORT NUMBER

9. SPONSORING / MONITORING AGENCY NAME(S) AND ADDRESS(ES)

U.S. Naval Academy
Annapolis, MD 21402

10. SPONSOR/MONITOR'S ACRONYM(S)

11. SPONSOR/MONITOR'S REPORT NUMBER(S)

Trident Scholar Report no. 532 (2023)

12. DISTRIBUTION / AVAILABILITY STATEMENT

This document has been approved for public release; its distribution is UNLIMITED.

13. SUPPLEMENTARY NOTES

14. ABSTRACT

Wave Energy Converters (WEC's) are devices that extract the energy stored in ocean waves and convert it into useful energy, like electricity. A cylindrical WEC was tested in both 1-degree-of-freedom (DOF) and 2 DOF configurations. The first set of experiments were performed with a 1 DOF system featuring mechanical springs which provided passive restoring forces. The second set of 1 DOF experiments and all of the preliminary 2 DOF trials were done with an actuated gantry. This gantry allowed for the control forces applied on the cylinder to be changed via software rather than by switching out mechanical hardware. During trials with wave amplitudes ranging from 0.75 inches to 1.5 inches and wave periods between 0.5 and 2.5 seconds, the hydrodynamic forces acting on the cylinder caused it to oscillate and absorb a fraction of the incident wave energy. The maximum energy available for extraction from the oscillator was 35% in the mechanical 1 DOF configuration, which occurred at the resonant wave period of 1.48 s and a wave amplitude of 0.75 in. Measurements of available energy for 1 DOF and 2 DOF tests with the gantry system are in the initial stages, as the presence of significant system frictional damping caused all experiments to have an overdamped response. However, the addition of a second degree of freedom caused an increase in available energy by a factor of around two (as compared to the 1 DOF gantry tests). Future work will consist of deducing an accurate model of gantry friction to allow the control system to properly account for it during experiments.

15. SUBJECT TERMS

Wave energy conversion, Control volume analysis, Linear wave theory, Renewable energy

16. SECURITY CLASSIFICATION OF:			**17. LIMITATION OF ABSTRACT**	**18. NUMBER OF PAGES**	**19a. NAME OF RESPONSIBLE PERSON**
a. REPORT	**b. ABSTRACT**	**c. THIS PAGE**		90	**19b. TELEPHONE NUMBER** *(include area code)*

U.S.N.A. --- Trident Scholar project report; no. 532 (2023)

Experimental Determination of Energy Absorption Characteristics of a Cylindrical Wave Energy Converter in Linear and Nonlinear Waves

by

Midshipman 1/C Ryan M. Conway
United States Naval Academy
Annapolis, Maryland

_____

Certification of Adviser(s) Approval

Professor Luksa Luznik
Mechanical and Nuclear Engineering Department

_____

_____

Associate Professor Levi DeVries
Weapons, Robotics, and Control Engineering Department

_____

_____

Acceptance for the Trident Scholar Committee

Professor Maria J. Schroeder
Associate Director of Midshipman Research

_____

_____

USNA-1531-2

Abstract

Wave Energy Converters (WEC's) are devices that extract the energy stored in ocean waves and convert it into useful energy, like electricity. A cylindrical WEC was tested in both 1-degree-of-freedom (DOF) and 2 DOF configurations. The first set of experiments were performed with a 1 DOF system featuring mechanical springs which provided passive restoring forces. The second set of 1 DOF experiments and all of the preliminary 2 DOF trials were done with an actuated gantry. This gantry allowed for the control forces applied on the cylinder to be changed via software rather than by switching out mechanical hardware. During trials with wave amplitudes ranging from 0.75 inches to 1.5 inches and wave periods between 0.5 and 2.5 seconds, the hydrodynamic forces acting on the cylinder caused it to oscillate and absorb a fraction of the incident wave energy. The maximum energy available for extraction from the oscillator was 35% in the mechanical 1 DOF configuration, which occurred at the resonant wave period of 1.48s and a wave amplitude of 0.75in. Measurements of available energy for 1 DOF and 2 DOF tests with the gantry system are in the initial stages, as the presence of significant system frictional damping caused all experiments to have an overdamped response. However, the addition of a second degree of freedom caused an increase in available energy by a factor of around two (as compared to the 1 DOF gantry tests). Future work will consist of deducing an accurate model of gantry friction to allow the control system to properly account for it during experiments.

KEYWORDS: wave energy conversion, control volume analysis, linear wave theory, renewable energy

Acknowledgements

I would like to thank CDR Li Sung and MIDN Brendan Neal for their help and contributions to this project. I would also like to thank the USNA Hydromechanics Laboratory Team for their guidance throughout the course of the project and their aid in setting up experiments. This project was funded by the National Science Foundation (Grant # 2135354).

Table of Contents

I. Introduction and Previous Work

A. Background

1. Importance

A wave energy converter (WEC) is a device that absorbs energy from ocean waves and converts it into useful energy, like electricity. This type of device has applications which include use in hydroelectric power plants, wave-breakers for harbors, and self-powered buoys/other marine equipment. WEC's are a very viable method of useful energy production. The Electric Power Research Institute (EPRI) has predicted that the US continental shelf could potentially produce upwards of 2640 TWh per year, with an average of 30-40 kW of power per meter of wave meeting the shoreline [1].

Modern renewable energy devices, namely marine current and wind turbines, typically absorb 40-45% of the flow energy incident to them. However, computer models [2] have predicted that a 2 degree-of-freedom cylindrical WEC (which is the device that will be investigated in this project) has potential for energy absorption efficiency up to 60%. For a dynamic system, a degree of freedom (DOF) is simply a way in which it can move. The degrees of freedom in this project are motions up/down (heave) and forward/back (surge). If the actual experimentally obtained efficiency of this device matches the predicted efficiency, it could have big implications for the renewable energy sector.

The objective of this project is to test a cylindrical wave energy converter (WEC) that has two degrees of freedom, focusing on its responses to linear and nonlinear waves.

2. Surface Gravity Waves

Since the excitation for wave energy converters is an oceanic wave, a description of a wave traveling on the free surface is necessary. This is a well-studied topic in the realm of fluid mechanics known as oscillatory flow. In a progressive wave, energy is transferred through water particles and propagates in a given direction. The water particles do not travel with the wave, instead they follow elliptical trajectories [3]. Figure 1 illustrates the important spatial characteristics of a surface gravity wave.

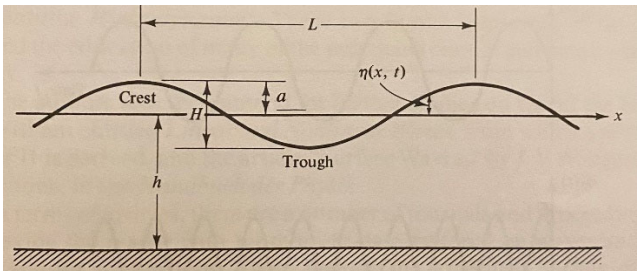

Figure 1: Relevant characteristic wave parameters. *L* is the wavelength of the wave, *H* is peak-to-peak wave height, *h* is the depth of the water, and *η* is the instantaneous position of the free surface [3].

Surface waves can be caused by a myriad of physical phenomena such as interactions with objects (e.g. waves generated by ships), seismic activity (tsunamis), the gravitational pull of the moon and sun (tidal waves) and wind-generated waves over an ocean surface. A noteworthy feature of surface waves is that as depth increases, the wave (oscillatory) velocity of fluid particles decays exponentially. In the context of a submerged cylinder this means that as cylinder depth increases, the oscillatory velocities of the incident waves decrease. Also, it is important to understand the difference between linear and nonlinear waves. Linear waves are governed by the Laplace equation, written as

$$\nabla^2 \phi = 0 \tag{1}$$

where ∇^2 is the Laplacian operator and ϕ is the velocity potential. Velocity potential is a simplification which describes irrotational ($\nabla \times \vec{v} = 0$) and incompressible flow, where $\vec{v}$ is the three-dimensional velocity vector field of a particle under the wave. This allows for an analytical solution to be found [2]. Solving this differential equation requires boundary conditions, and two of these boundary conditions (the dynamic free surface boundary condition and the kinematic free surface boundary condition) involve truncating a Taylor series expansion of the Bernoulli equation to the first order. This process is called linearization, and is only appropriate for small-amplitude waves. However, when dealing with waves that have larger amplitudes, the higher-order terms cannot be ignored. These waves are called nonlinear waves.

Nonlinear waves are prone to breaking, which is an event where a wave becomes unsteady and crashes onto itself. A useful parameter that is used to classify waves in pre-breaking condition is known as wave steepness, which is defined as the ratio between wave height (amplitude) and wavelength [4]. It can also be expressed in non-dimensional terms as the product of wave amplitude and wavenumber, where wavenumber is defined as $k = 2\pi / L$ (L is the wavelength). Above a wave steepness of 0.13, the wave becomes unsteady and is susceptible to breaking [5]. Nonlinear waves are characterized by steepnesses larger than this critical steepness.

A second-order solution to the Laplace equation has been developed by Stokes [3], but it does not represent waves well in their pre-breaking phase. For comparison, Figure 1 is a representation of a small-amplitude wave and Figure 2 shows the three main stages of wave breaking: growth, breaking inception and breaking event. The latter is relevant to this project since it has been observed that when linear (small-amplitude) waves approach shallow water (or experience a “beaching” effect from hitting a cylinder) they grow in amplitude and become prone to breaking [3].

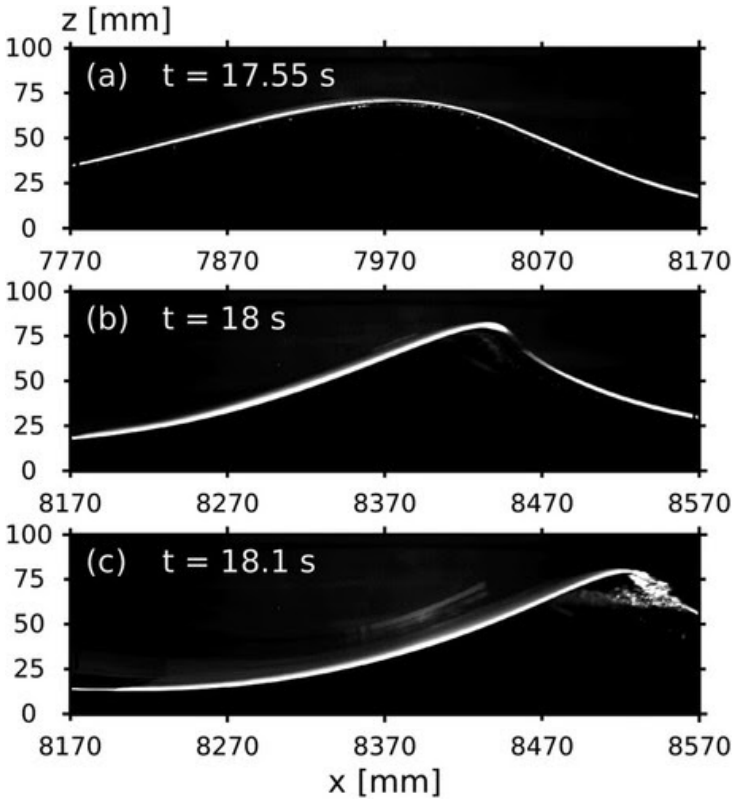

Figure 2: Top: wave growth stage, Middle: inception of breaking, Bottom: breaking event [6].

3. Submerged Cylinder in Uniform Flow

The drag experienced by a submerged cylinder in uniform flow and the resultant wake structure has been studied extensively. Drag can be thought of as a product of the shape, orientation, and material of the object in the fluid field. There are two terms that make up total drag force on a submerged object: pressure drag and friction drag. The magnitude of pressure drag is directly related to the momentum deficit of the fluid (i.e. the difference in momentum of the fluid before the fluid strikes the object and after, as seen in the wake). Friction drag accounts for the drag caused by the fluid molecules "pulling" the object in the direction of flow. The drag on a submerged cylinder is a function of the Reynolds number (Re) of the flow, which is a dimensionless parameter related to the speed of the flow and the physical properties of the system (discussed further in section I.B). Figure 3a displays the dimensionless drag coefficient C_d on a submerged cylinder as a function of Re, and Figure 3b highlights rich wake structures developing in the cylinder near wake as a function of increasing Re.

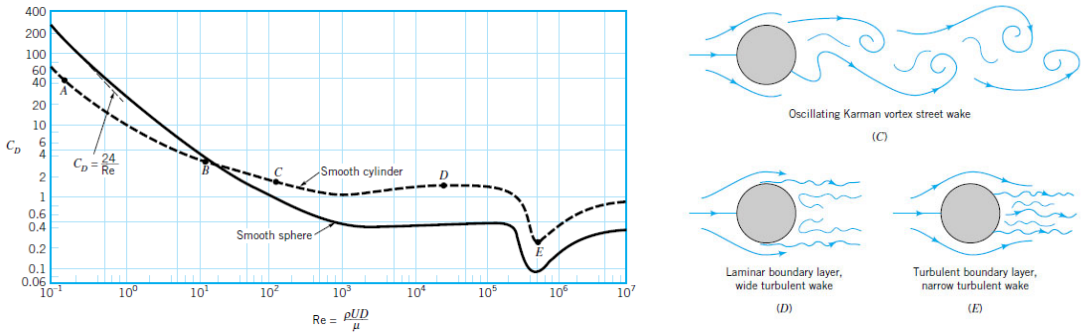

Figure 3: a: Plot of drag coefficient vs. Reynolds number for submerged cylinder (dotted curve). b: Depictions of different wake structures corresponding to state points on graph 1a [7].

Figure 3a highlights the general trend in drag coefficient as the Re of the flow increases. It is worth noting that state points A and B are not relevant to this project, as they represent flow conditions much slower than what will be seen in the project. At Point C, which corresponds to a Re of just over 100, the wake is wide and characterized by oscillating Karman vortices, which are a form of vortex shedding. However, at point E, or Re=5x10^5, the wake is much narrower and characterized by the presence of turbulence. A narrower wake means there is a smaller momentum deficit, which means there is less pressure drag but still a significant frictional drag due to a turbulent boundary layer developing on the cylinder surface.

4. Submerged Cylinder in Uniform Flow Near Free Surface

The effects of uniform flow on the wake of a submerged cylinder change when the cylinder is brought close to the free surface. Proximity to the free surface introduces new wake structures that change based on distance between the top of the cylinder and the free surface. It has been shown experimentally that in flow with Re =170, the wake of a cylinder that is close to the free surface exhibits a single narrow stream of unsteady vortices [8]. This is because the free surface starts to distort (see Figure 3 below) and can result in free surface breaking. However, when the distance between the top of the cylinder and the free surface increases the wake structure starts resembling that of a completely submerged cylinder (Karman vortices). As mentioned previously, changes in wake structure correlate to a change in drag on the cylinder. As the depth of the cylinder decreases, the drag of the cylinder decreases quickly after initially increasing [8].

B. Theoretical Basis

1. Scaling

To perform an experiment that yields meaningful results, scaling between the experimental model and full-size prototype must be considered. Scaling is done with the use of dimensionless parameters, and different applications require the use of different dimensionless parameters in order to scale properly. When investigating the effects of flow over a submerged cylinder near the free surface, the three parameters used are the Froude number, the immersion depth and the aforementioned wave steepness. The Froude number takes the form

$$F_r = \frac{U}{\sqrt{gD}} \tag{2}$$

Where U is the free stream velocity of the fluid, g is acceleration due to gravity and D is the diameter of the submerged cylinder. An interpretation of the Froude number is that it is the ratio of the inertia force on an element of fluid to the weight of the element. This parameter is used in experiments that involve flows with free surfaces because gravity has a large impact on these flows [3]. In this project, the Froude number of incident waves will be used (rather than the Froude number of the cylinder wake). Immersion depth is expressed as h / D, where h is the distance between the top of the submerged cylinder and the free surface [9]. Figure 4 presents a visual of the relevant parameters used for scaling in this project.

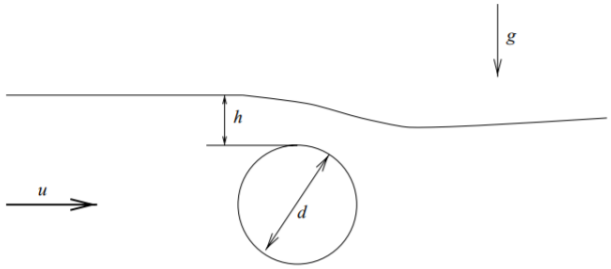

Figure 4: Illustration of relevant parameters for experimental scaling [8].

For the results of the experiment to be applied to an apparatus with different design parameters (i.e. a full-size version), the Froude number, immersion depth and wave steepness of the full-size (prototype) version must be equal to the Froude number, immersion depth and wave steepness of the model. This can be represented as

$$F_{r,full} = F_{r,model} \quad , \quad \frac{h_{full}}{D_{full}} = \frac{h_{model}}{D_{model}} \;\; \& \;\; kA_{w,full} = kA_{w,model} \tag{3}$$

In this project, the "prototype" waves that are being scaled are intermediate and deep waves typically found off of the US eastern seaboard continental shelf. For example, using wave steepness scaling, a 1in amplitude wave having a wavelength of 2.5m (which can be easily created in the USNA Hydromechanics 120ft and 380ft tow tanks) represents a full-scale wave with 1m amplitude and 100m wavelength.

2. Reynolds Number

Another non-dimensional term that is relevant in nearly all applications of fluid mechanics is the Reynolds number, which is described as

$$Re = \frac{\rho UD}{\mu} \quad \text{or} \quad Re = \frac{UD}{\nu} \tag{4}$$

Where ρ is the density of the fluid, μ is its dynamic viscosity, and ν is its kinematic viscosity. It can be thought of as the ratio of the inertia force on an element of fluid to the viscous forces on that same element. This term is not used to scale experimental results of fluid flow over a cylinder near the free surface because it is not possible to scale via a Reynolds number and Froude number concurrently. When scaling to a projected full-size prototype from a model, the Reynolds number and Froude number will give you different free stream fluid velocities. However, the Reynolds number is still extremely useful for describing and understanding the properties of a given fluid flow. It can be defined in different ways depending on the desired area of investigation. For example, if a macroscopic view of the flow over the cylinder is desired, the

Reynolds number should be defined using the free stream velocity as mentioned above. However, if there is a specific region of flow that needs to be analyzed (like within the boundary layer of the cylinder), the local Reynolds number can be defined as $Re_L = \rho u_L D / \mu$ or $Re_L = u_L D / \nu$, where u_L is the local fluid velocity and the subscript L signifies the local characteristics.

3. Forces on Oscillating Cylinder

The oscillation of a cylindrical WEC occurs due to forces brought on by incident waves. Total wave force per unit length of the cylinder is the combination of drag and wave inertia, and is summarized by the Morrison equation [3]:

$$dF = dF_D + dF_I \tag{5}$$

Where the forces are represented in differential form. dF_D is the differential force of the wave on the object due to drag, and dF_I is the differential force of the wave on the object due to wave inertia, or motion. This term is derived by integrating the pressure distribution around the cylinder. It can be found that the drag force (also known as the "steady" term, because it is a function of fluid free-stream velocity) can be parametrized as

$$dF_D = \frac{1}{2} C_d \rho (U(t))^2 A \tag{6}$$

Where A is the projected area of the cylinder per unit length and C_d is a function of Re. Using the aforementioned potential flow solution, the inertia force, or the "unsteady" term (as it is a function of $\frac{dU}{dt}$) is

$$dF_I = C_M \rho dV \frac{dU}{dt} \tag{7}$$

Where C_M is the inertia coefficient and V is the volume of the cylinder per unit length. The inertia coefficient is found using $C_M = 1 + a_m$, where a_m is the added mass [3]. Added mass accounts for the increase in inertia of the cylinder caused by the fluid [10].

4. Evans Linear Wave Theory

Work by Evans [10] in the 1970's on a 2 DOF wave energy converter system forms a starting point for this project. Evan's system consisted of a neutrally buoyant cylinder (oscillator) placed perpendicular to the direction of the incident waves. Evans proved through linear wave theory that if the oscillator was driven by linear, constant frequency waves, it had the potential to absorb 100% of the incident waves' energy (assuming that the absorbed energy could be properly and efficiently converted into useful energy).

Evans also provided relations for the optimum WEC mechanical spring stiffness and damping coefficient required to produce system resonance for a given incident wave frequency. Evans found that the stiffness of the spring and damping coefficient should be

$$k = [m + (a_m(\omega))]\,\omega^2 \;\&\; c = \frac{1}{2}\rho\omega|A_w|^2(1-\delta(\omega))^{-1} \tag{8}$$

Where k is the spring stiffness, m is the mass of the cylinder, a_m is the aforementioned added mass, ω is the incident wave frequency, c is the damping coefficient, ρ is the density of the fluid, A_w is the amplitude of the incident wave, and δ is a quantity related to the geometry of the

cylinder which varies with frequency. Springs and dampers found according to equation (8) allow a WEC to oscillate with a maximum displacement response at the same frequency as the incident waves (assuming the incident waves are regular waves with a single frequency). This is known as resonance. It has been shown that WEC's achieve their highest energy absorption when operating at resonance [10].

One final noteworthy piece of the Evans wave absorption theory is the choice of optimal depth for the WEC if placed near the free surface. This depth is

$$h = \frac{5}{4}r \tag{9}$$

Where r is the radius of the cylinder [10]. Figure 5 highlights the important aspects of the Evans Linear Wave Theory.

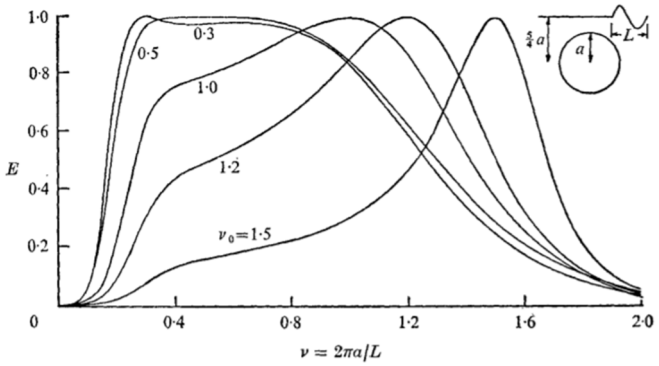

Figure 5: Energy absorption efficiency vs ratio of cylinder radius to incident wavelength [2].

The sketch on the top right of the figure indicates that the results corresponded to a WEC that was submerged to the previously mentioned depth of $\frac{5}{4}r$. Each of the curves represents a different WEC spring stiffness/damping coefficient combination, demonstrating the impact that spring stiffness and the damping coefficient have on WEC performance. All of the curves reach an energy absorption efficiency of unity at their respective resonant states.

5. System Model

The cylindrical WEC system (1 DOF configuration) can be modeled by a spring-damper system, as shown below in Figure 6:

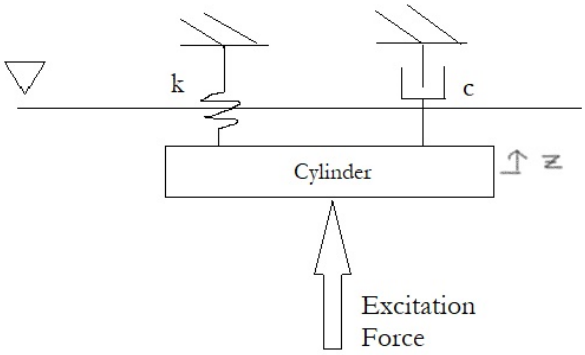

Figure 6: Spring-Damper model of 1 DOF WEC system.

The equation of motion for this 1 DOF system is

$$m\ddot{z} = F_{exc} + F_{damp} + F_{spring,cont} \tag{10}$$

Where m is the mass of the submerged cylinder (including mass of water inside of the cylinder cavity), $\ddot{z}$ is the acceleration of the cylinder in the heave axis, F_{exc} is the force on the cylinder due to the incident waves, F_{damp} is the total damping force experienced by the cylinder and $F_{spring,cont}$ is the spring force on the cylinder provided by the control system (related to spring constant k in equation (8)). The total damping force term can be broken down into 3 components as shown in equation (11):

$$F_{damp} = F_{visc} + F_{damp,cont} + F_{PTO} \tag{11}$$

Where F_{visc} is the viscous drag opposing the motion of the cylinder, $F_{damp,cont}$ is the damping force provided by the control system which is related to the fact that the oscillating cylinder will create a wave field that radiates away from the cylinder, and F_{PTO} is the damping force applied by the power takeoff device (machinery). In this project there is no power takeoff system as this is an early stage of the overall USNA wave energy conversion project, so for now and throughout this Trident project $F_{PTO} = 0$. The total hydrodynamic force on the cylinder can be defined as

$$F_{hydro} = F_{exc} + F_{visc} \tag{12}$$

Therefore, the final equation of motion for a 1 DOF oscillator can be written as

$$m\ddot{z} = F_{hydro} + F_{damp,cont} + F_{spring,cont} \tag{13}$$

For simplicity, linearization of equation (13) results in $F_{damp,cont}$ and $F_{spring,cont}$ being found using equation (14):

$$F_{spring,cont} = -k * z \;\; \& \;\; F_{damp,cont} = -c * \dot{z} \tag{14}$$

This is to say that the spring restoring force is related to the cylinder displacement through a linear spring constant k and the radiated cylinder wave field is related to the damping coefficient c found in equation (8). For a system that possesses a second degree of freedom, equations (13) and (14) can be applied in both axes.

II. Experimental Setup

A. Apparatus Designs/Setups

Experiments were completed during March 2022 – March 2023 in the USNA Hydromechanics Laboratory 120ft and 380ft tow tanks with two system configurations: an undamped mechanical spring system fixed to a single degree of freedom (heave) and a linear motion gantry capable of operating in both 1 DOF and 2 DOF configurations. Experiments done in the 120ft tank elucidated the 2-D effects of wave forcing on the cylinder, as the cylinder was essentially as wide as the tank itself (12mm between the cylinder and walls on each side). Experiments done in the 380ft tank elucidated the 3-D effects of wave forcing on the cylinder, as the cylinder was much shorter than the tank was wide (edge effects started to become prevalent). The mechanical undamped spring system was tested in both the 120ft and 380ft tanks, while the gantry system was only tested in the 380ft tank.

1. Undamped Mechanical Spring System

A Solidworks model of the system, as well as the schematic of the undamped mechanical spring system mounted in the 120ft tank, is shown in Figure 7.

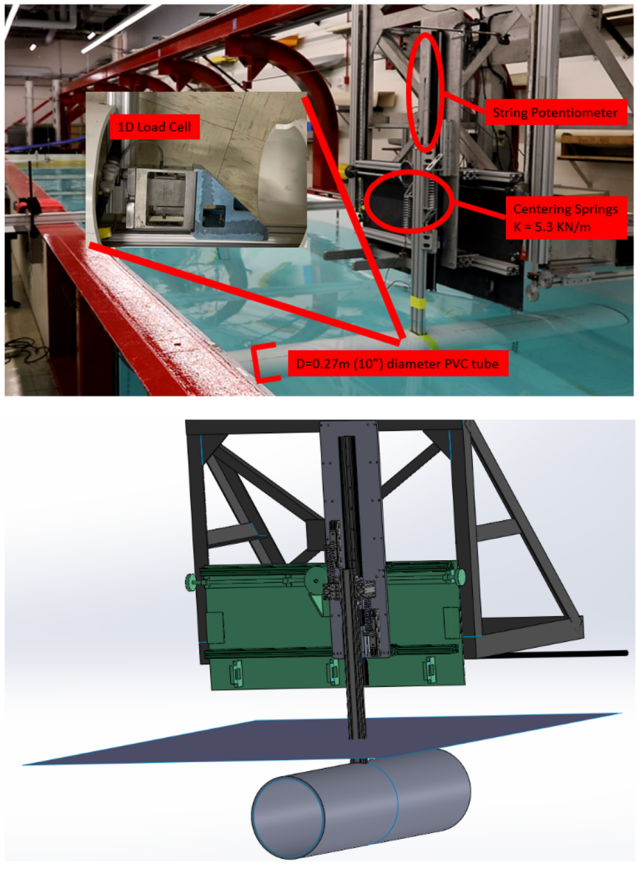

Figure 7: Schematic of mechanical undamped spring system setup in 120ft tank (top), Solidworks model of system (bottom).

The cylinder was made of hollow PVC pipe with an outer diameter of 0.27m and a length of 2.375m. Two mechanical springs were used to provide restoring forces to the system and set system resonance at a period of 1.48s. To achieve this, equation (8) was used and it was found that a spring stiffness of 5.3 kN/m was required. A restoring damper was not used in this setup. A string potentiometer was used to find instantaneous cylinder vertical displacement (i.e. z-displacement), and a load cell situated inside of the cylinder was used to measure hydrodynamic excitation force acting on the cylinder in the vertical (z) direction. To allow for motion in the vertical axis, a linear motion rail was utilized along with two low-friction sleds that connected the cylinder sting to the rail. Additionally, a single camera was set up on the side of the tank to record footage of the cylinder oscillating through a window on the side of the tank.

2. Gantry System

The configuration of the gantry system setup in the 380ft tank is shown in Figure 8. Like the mechanical undamped spring system, the gantry also utilized a vertical sting to connect the cylinder to the gantry end effector.

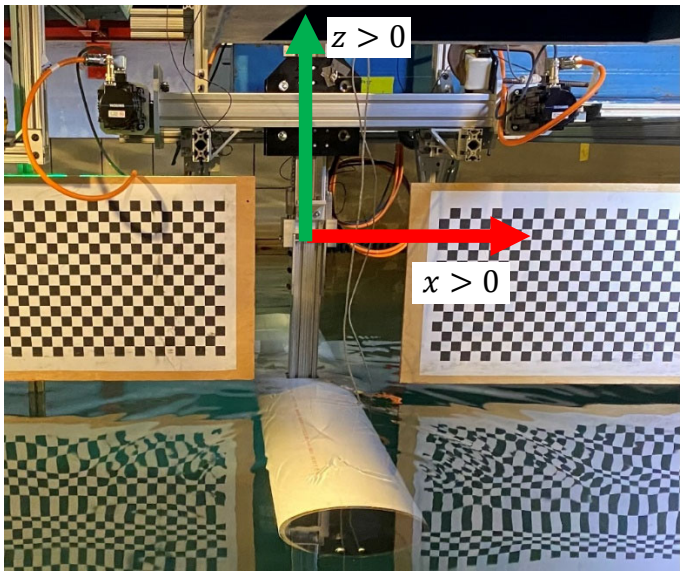

Figure 8: Picture of linear motion gantry system set up in 380ft tank, with checkerboard plates for camera calibration.

To allow for gantry actuation and control, two 2.5 kW servo motors were connected to the gantry via gear boxes that had 10:1 gear ratio's (output torque divided by input torque). Two string potentiometers were used to measure the displacement of the cylinder in both the surge (x) and heave (z) axes. Two load cells located in the body of the cylinder were used to measure the force felt by the cylinder in both the surge and heave axes. The load cells used were Hydronautics Modular Force gages Model HI-M-4. A 500lb max force cell was used for the heave axis and a 250lb max force cell was used for the surge axis, and the reason for this difference was due to availability of load cells in the USNA Hydromechanics Laboratory. The placement of the load cells in the cylinder was not a trivial matter. They had to be placed in a manner that allowed for the force to travel in a path directly through both cells. The final configuration of the load cells is shown in Figure 9:

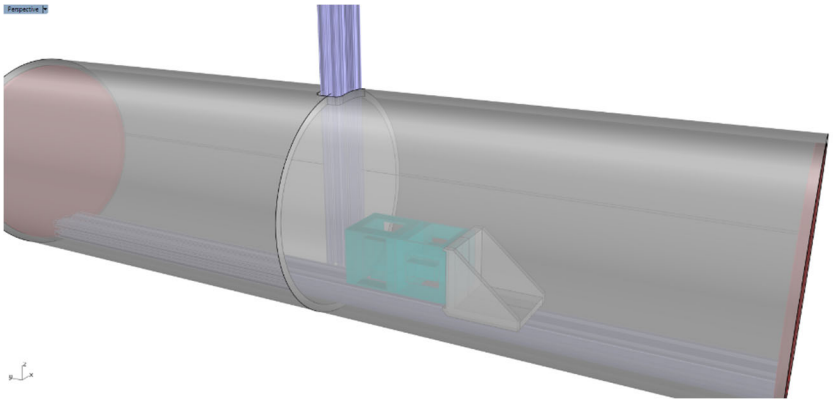

Figure 9: Schematic of load cell configuration inside of cylinder.

The load cell measuring force in the heave axis was fixed to the sting, the load cell measuring force in the surge axis was fixed to the heave cell and a bracket connected the cells to the longitudinal support beam. This created a direct path for the hydrodynamic force on the cylinder to travel from the support beam through the bracket and into the load cells, where it then traveled to the sting.

i.) Motor Kinematics/Dynamics

To calculate the motor torque required to provide the cylinder with the desired restoring forces, the kinematics of the belt driven gantry were derived to estimate the applied forces at the end effector. The motor coordinate system was based on the circumferential travel of the motor shafts, with a counter-clockwise rotation being positive. Figure 10 shows the schematic of the motor-end effector coupling provided by the gantry manufacturer, Macron Dynamics.

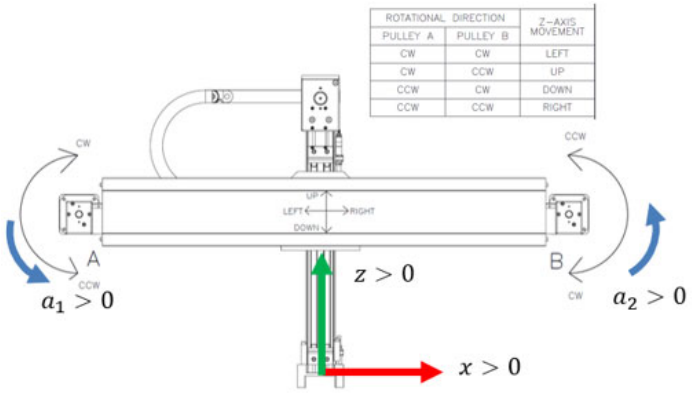

Figure 10: Schematic of motor-end effector coupling.

Assuming zero slip in the belt, pulleys, gearboxes, and slides, the kinematic relationship between the motor shaft positions a_1 and a_2 measured in circumferential units (mm) and the coordinates of the end effector position (x, z) in mm are:

$$\begin{bmatrix} a_1 \\ a_2 \end{bmatrix} = \begin{bmatrix} 1 & -1 \\ 1 & 1 \end{bmatrix} \begin{bmatrix} x \\ z \end{bmatrix}$$

$$a_1 = x - z \tag{15}$$

$$a_2 = x + z$$

Where x is the position of the end effector in the surge axis, z is the position of the end effector in the heave axis and a_1, a_2 are the circumferential position of each motor shaft. Similarly, assuming no frictional or efficiency losses in the belt, slides and gearboxes, forces on the end effector were related to torques at the motor output shaft by:

$$\begin{bmatrix} \tau_1 \\ \tau_2 \end{bmatrix} = \frac{R}{10} \begin{bmatrix} 1 & -1 \\ 1 & 1 \end{bmatrix} \begin{bmatrix} f_x \\ f_z \end{bmatrix}$$

$$\tau_1 = \frac{R}{10}(f_x - f_z) \tag{16}$$

$$\tau_2 = \frac{R}{10}(f_x + f_z)$$

Where f_x and f_z are the desired control forces in each axis calculated using equation (14), R is the radius of the gantry drive pulley shaft and τ_1, τ_2 are the required input torques for each motor. The right side of each torque equation is divided by 10 to account for the 10:1 gear ratio at each gearbox.

ii.) Tracking of Surface Wave Field in Vicinity of Oscillator

Additionally, three high speed cameras (Fastec TS5's) were mounted to the tow tank carriage to record the free surface profile. In order to accomplish this, Laser Induced Fluorescence (LIF) was used, which is described in section IV.B. The checkerboards on each side of the gantry (shown in Figure (8)) were used to calibrate these cameras and allow for a conversion from image frame pixel units to world frame length units. Figure 11 shows the setup of the cameras in the 380ft tank used in experiments done with the linear motion gantry system. Each camera had a field of view of approximately 2m in the x direction and 0.5m in the z direction.

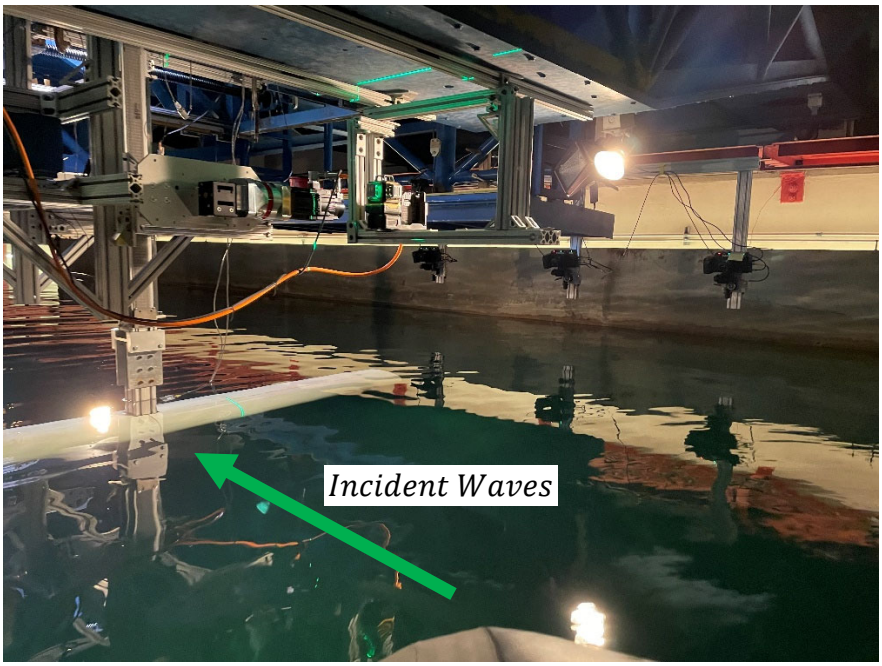

Figure 11: Image of camera setup used during gantry experiments.

The cameras were mounted to vertical lengths of 80/20 aluminum extrusion with an adapter that allowed for fine attitude adjustment. One camera recorded footage of the free surface 2m upstream of the cylinder, one recorded the free surface directly above the cylinder and the last camera recorded the free surface 2m downstream of the cylinder.

B. Wave Tank Setup

Figure 12 shows a schematic of the tank setup for each set of experiments.

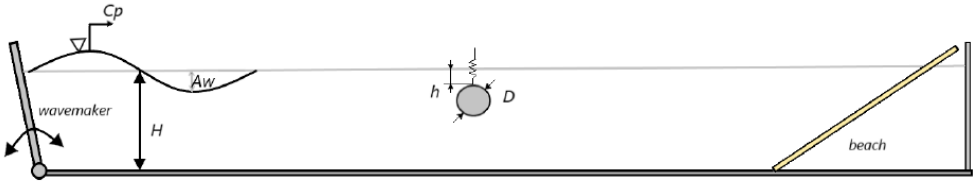

Figure 12: Schematic of experimental setup.

For the experiments done with the mechanical undamped spring system, three wave probes were used: one directly aft of the wavemaker, one 2m upstream of the cylinder and the last one 2m downstream of the cylinder. For the experiments done with the gantry setup, 5 probes were used: One directly aft of the wavemaker, one 12m upstream of the cylinder, one 3 m downstream of the cylinder, one 12m downstream of the cylinder and one 24m downstream of the cylinder. Figure 13 shows the schematic of the wave probes used in the gantry experiments.

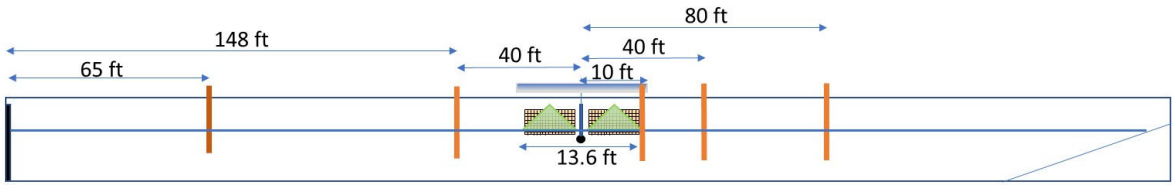

Figure 13: Schematic of wave probe setup for gantry experiments.

Additional wave probes were added for these runs to provide a better understanding of the impact of the cylinder on the incident wave field. For each set of experiments, the apparatus was subject to waves with periods ranging from 0.5s to 2.5s and amplitudes varying between 0.75in to 1.5in. This corresponded to incident wave steepnesses ranging between $0.018 \leq kA_w \leq 0.22$ for the mechanical spring setup and $0.026 \leq kA_w \leq 0.11$ for the gantry setup. The reason for the difference in these two ranges is that due to time constraints, only experiments done with linear incident waves were able to be performed with the gantry setup. For each trial, 60s of data was taken in the 120ft tank and 90s of data was taken in the 380ft tank. The difference in sample times in the two tanks came from the presence of wave reflection from the beach. In the shorter tank, the downstream probe was contaminated by reflected waves sooner. Therefore, a smaller amount of useful data was able to be collected.

Data from each measurement system was collected using National Instruments hardware. Data collection was interfaced through MATLAB and the data for each trial was written to an excel sheet. These excel sheets were then loaded into MATLAB for analysis.

III. Data Analysis

A. Control Volume Approach

The data analysis for this project was done using a control volume (C.V.) approach. In order to understand how this approach works, some wave energy theory is needed. The total energy of a wave per unit surface area is represented as $E = \frac{1}{8}\rho g\overline{\eta^2}$, where $\overline{\eta^2}$ is the variance of the average peak-to-peak wave amplitude as measured by a wave probe. This is found using the equation $\overline{\eta^2} = \frac{1}{t_2 - t_1}\int_{t_1}^{t_2} {A_w}^2 dt$, where $t_2 - t_1$ is the length of the sampling interval. Another way to think of the variance is as the average value of the square of incident wave amplitude over the sampling interval. The corresponding energy flux of the wave (per unit surface area), or the rate at which energy flows through a boundary, is $F = \frac{1}{8}\rho g\overline{\eta^2}C_g$, where C_g is the wave group speed. Wave group speed is the speed of the incident wave envelope. Wave energy flux travels at the group speed of the wave [3]. For the purposes of data analysis, wave measurements at the upstream probes are denoted with an "o" and wave measurements at the downstream probe are denoted with a "D". The crux of the C.V. method is that the energy dissipated in a given volume of fluid (in this case, the region between upstream and downstream locations) can be calculated by finding the difference between the energy that enters the control volume and the energy that leaves the control volume. Figure 14 shows the control volume used in this experiment.

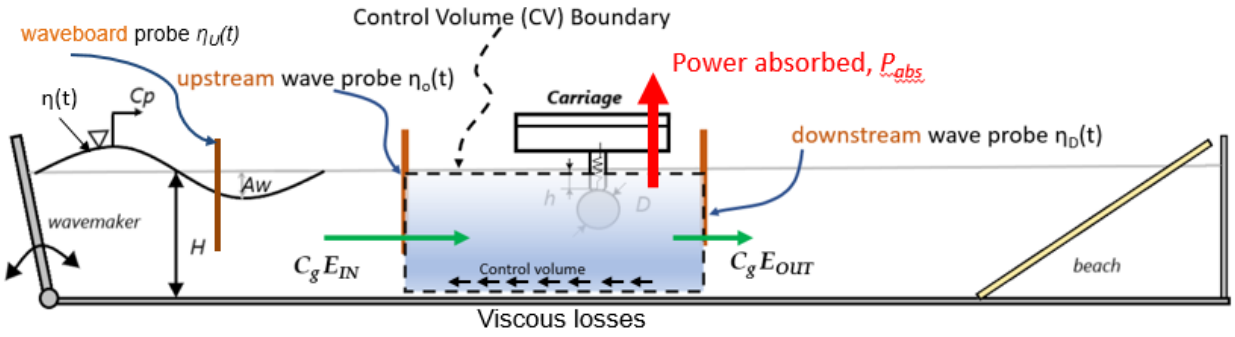

Figure 14: Schematic of control volume used in analysis.

The change in energy flux between the upstream and downstream locations (with the difference corresponding to the energy dissipated in the control volume) is

$$\Delta F = \frac{1}{8}\left[\int_{t_1}^{t_2} C_{go}\ \rho\ g\ \overline{\eta_o^2}\ dt - \int_{t_1}^{t_2} C_{gD}\ \rho\ g\ \overline{\eta_D^2}\ dt\right] \tag{17}$$

It was assumed that $C_{go} = C_{gD} = C_g$. To make the data easier to interpret, the amount of energy dissipated in the control volume was represented as a fraction of ΔF to the initial incident energy flux. This fraction was written as

$$\epsilon_D = \frac{\overline{\eta_o^2} - \overline{\eta_D^2}}{\overline{\eta_o^2}} \tag{18}$$

Thus, the quantity ϵ_D in principle includes the energy absorbed by the oscillator and the energy loss due to viscous shear stress at the walls of the control volume and energy loss due to wave breaking (caused by aforementioned beaching effect).

The average power absorbed by the cylinder was found using

$$P_{abs} = \frac{1}{t_2 - t_1}\int_{t_1}^{t_2} F_z v_z\ dt + \frac{1}{t_2 - t_1}\int_{t_1}^{t_2} F_x v_x\ dt \tag{19}$$

Where F_z is the hydrodynamic excitation force on the cylinder in the heave axis, F_x is the hydrodynamic excitation force on the cylinder in the surge axis, v_z is the velocity of the cylinder in the heave axis, v_x is the velocity of the cylinder in the surge axis and $t_2 - t_1$ is the size of the sampling interval, which for this experiment was 20s. The hydrodynamic force on the cylinder in each axis was found using equation (20):

$$F_{hydro} = F_{LoadCell} - (F_{spring,cont} + F_{damp,cont}) \tag{20}$$

Where $F_{LoadCell}$ is the force reading pulled directly from the load cells located inside of the submerged cylinder.

The fraction of incident wave energy available for extraction by the WEC was calculated using equation (21):

$$E_{available} = \frac{P_{abs}}{P_{incident}} \tag{21}$$

Incident wave energy flux (or power) $P_{incident}$ was found using $P_{incident} = \frac{1}{2}\rho\, g\, A_w\, C_g$, where A_w is the amplitude of the incident wave. The calculated energy available for extraction can be thought of as the fraction of incident wave energy that is available for a hypothetical power takeoff system (machinery) to harness.

IV. Results

A. Mechanical Undamped Spring System

Figure 15 shows how available cylinder power, displacement and velocity look from numerical simulations. WECSIM (Wave Energy Converter Simulator) [15] was used, which utilizes hydrodynamic data from boundary element method (BEM) software Capytaine and produces the time series response of the device for a given wave frequency.

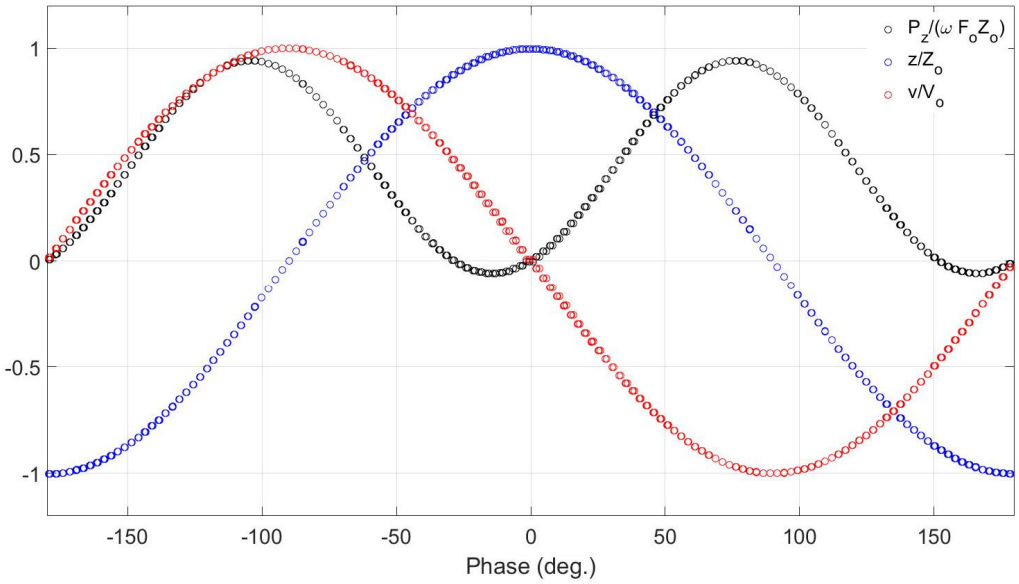

Figure 15: Normalized instantaneous cylinder position, velocity and power as a function of phase angle for undamped 1 DOF oscillator using WECSIM at resonance ($A_w = 0.75$ in, $T_w = 1.48s$).

The instantaneous cylinder power (black circles) was normalized by dividing each data point by the average available power in heave, which was found using equation (22) [13]:

$$P = \frac{1}{2}\omega_w z_0 F_0 \tag{22}$$

Where ω_w is the frequency of the incident waves, z_0 is the amplitude of cylinder displacement and F_0 is the amplitude of the wave excitation force F_{hydro} on the cylinder. The instantaneous cylinder position (blue circles) was normalized by dividing it by z_0 and the instantaneous cylinder velocity (red circles) was normalized by dividing it by v_o, or the amplitude of the cylinder velocity.

Figure 16 shows the **measured** instantaneous cylinder position, velocity and power as a function of instantaneous phase angle for the undamped mechanical system normalized as

discussed above. Instantaneous phase was obtained by applying the Hilbert Transform to the cylinder displacement data as per [14]. This plot shows the data over 15 wave cycles during the same experimental trial.

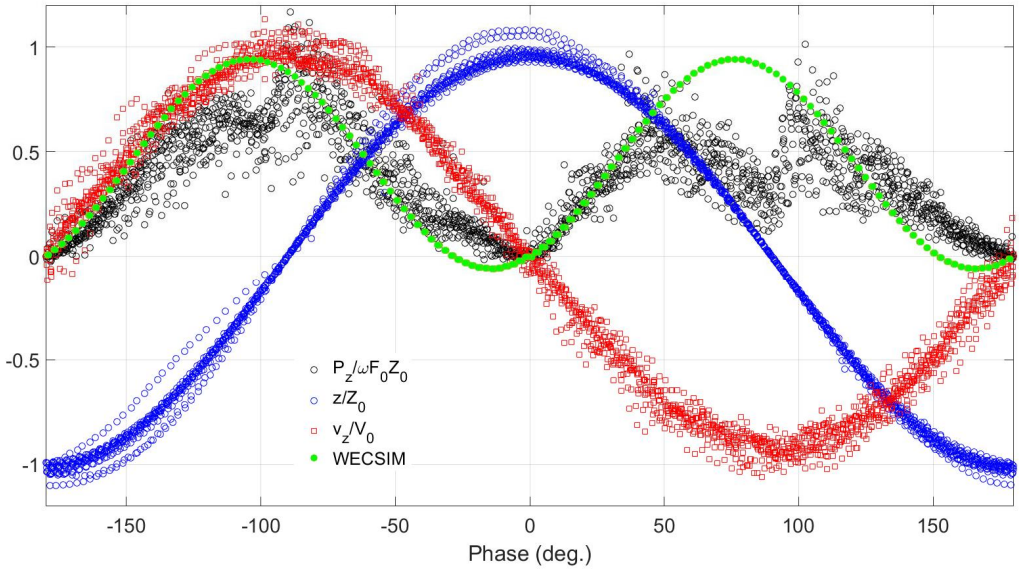

Figure 16: Normalized instantaneous cylinder position, velocity and power as a function of phase angle for undamped mechanical spring system at resonance condition ($T_w = 1.48\ s$) and $A_w = 0.75$ in. Green line is the power curve from WECSIM numerical model.

Figure 16 shows that cylinder power has two peaks during one displacement cycle. These peaks line up with maximum magnitudes of cylinder velocity. Cylinder power is zero when system displacement is at a maximum magnitude, which makes sense because the velocity is zero at these points. The WECSIM power shows slight deviation from experimental power globally and more pronounced deviation at the second power peak. WECSIM does not account for viscous flow or damping of any kind, which could explain the slight global deviation. The hypothesis for why the experimental cylinder power scatters near the max value at the second peak is that it was due to system buoyancy. The cylinder was not quite neutrally buoyant, as it favored positive buoyancy (floating to the surface). As the system started to move deeper into the water (phase angle between 50-100 degrees on the plot) The buoyant force resisted this motion and affected power output at this point in the cycle.

Now that it is understood how available power looks at one frequency (resonance), it is of interest to show the spectrum of available power obtained experimentally at a range of incident wave frequencies. This is shown in Figure 17 for 0.75in incident wave amplitude for two different configurations: measurements in the 120ft tank – 2D configuration, and 380ft tank measurements – 3D configuration. The energy available for extraction is represented as η on the y-axis for all control volume analysis plots in this paper.

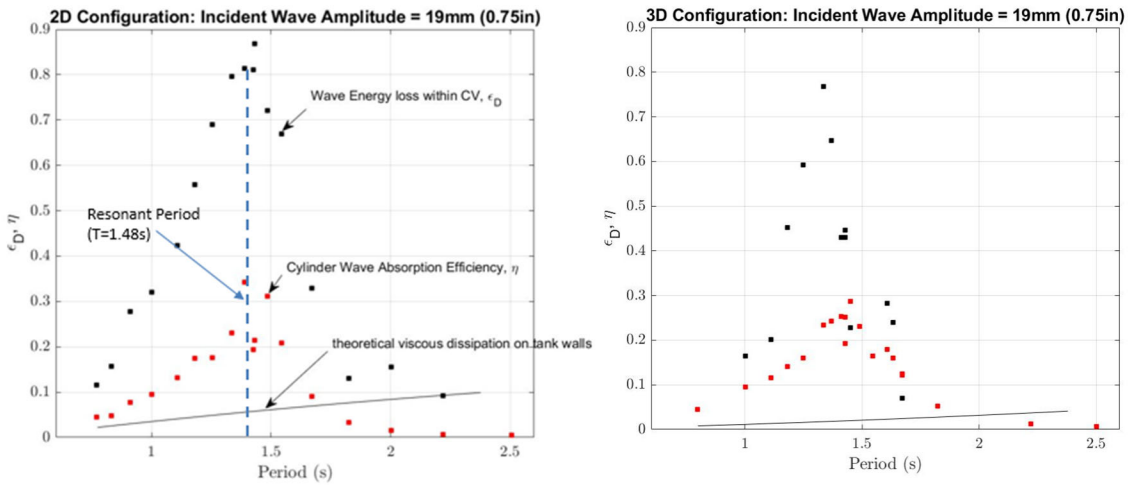

Figure 17: Control volume analysis results for 0.75in incident waves. The horizontal axis is the wave period (s) and the vertical axis shows the wave energy dissipated in the control volume ϵ_D (equation 18) and fraction of incident wave energy available for extraction (equation 22).

When looking at the short and long waves for the 2-D configuration (low and high wave periods) the summation of the theoretical viscous dissipation and available energy for absorption by the cylinder equals just about all of the total energy dissipated within the control volume. However, this is not the case for the resonant condition. The reason for this is that the system operated only in one degree of freedom and thus there was lots of leftover wave energy that was not extracted. The maximum value of energy dissipation in the control volume was found to be 90% at resonance, and the maximum value of available energy for extraction was 35% at resonance. As for the 3-D configuration, the maximum available energy for extraction was 29% and the maximum energy dissipation was 78%, both at resonant conditions. Also, a sharp drop-off in wave energy dissipated in the control volume is quite apparent just past the resonant conditions. This trend is further exemplified for incident waves with a larger amplitude of 1.25in, shown in Figure 18.

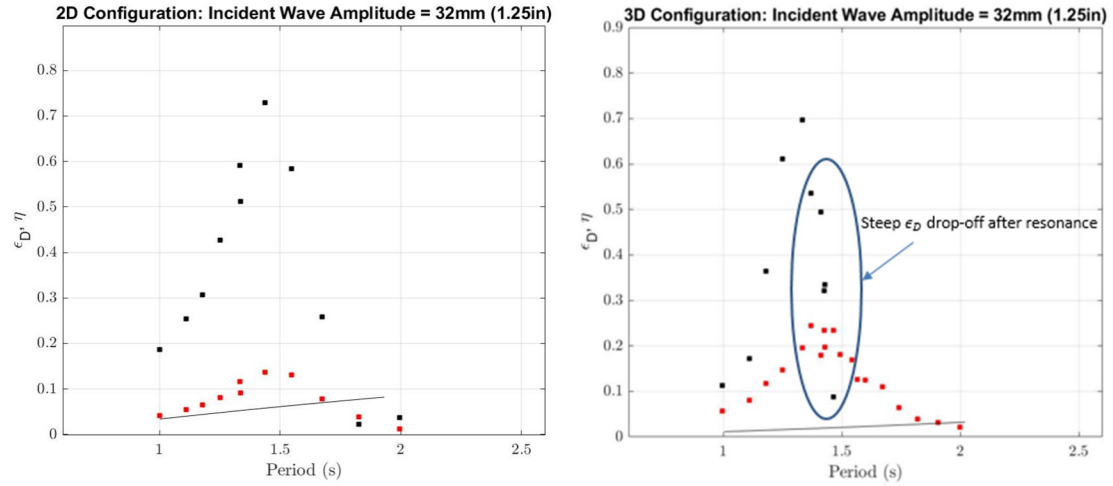

Figure 18: C.V. analysis results for 1.25in incident waves.

For the 2-D configuration, the maximum energy available for extraction was just 15%, which is a 57% decrease from the 0.75in waves in the 2-D configuration. It is postulated that the drop in available energy was caused by the onset of nonlinearities seen with higher-amplitude incident waves. The maximum control volume wave energy dissipation was 73%, which is a 19% decrease from the 0.75in waves in the 2-D configuration. Thus, incident wave interaction with the cylinder resulted in less wave energy lost in the control volume. Consequently, this resulted in smaller amounts of available energy from the device. As mentioned previously, the steep drop-off in wave energy dissipated within the control volume is further accentuated by the 3-D configuration as seen in Figure 18. The reason for this drop-off is a "lens focusing" effect, where the waves refract around the edges of the cylinder and meet at a point in the wake of the cylinder. This causes the wave group speed to decrease and the local wave amplitude to increase. This also explains the non-physical points present in the analysis results. These points are ones in which the total fraction of energy dissipated within the control volume is smaller than the fraction of available energy from the cylinder. This demonstrates the assumption of a constant wave group speed breaking down for higher-amplitude waves past the resonant condition. For the 3-D configuration, the maximum available energy for extraction was 25%, which is a 14% decrease from the 0.75in waves in the 3-D configuration.

In order to gain insight into the wave field at the control volume boundaries, Figure 19 displays the wave steepnesses from the upstream wave probe for incident wave amplitudes of 0.75in and 1.25in.

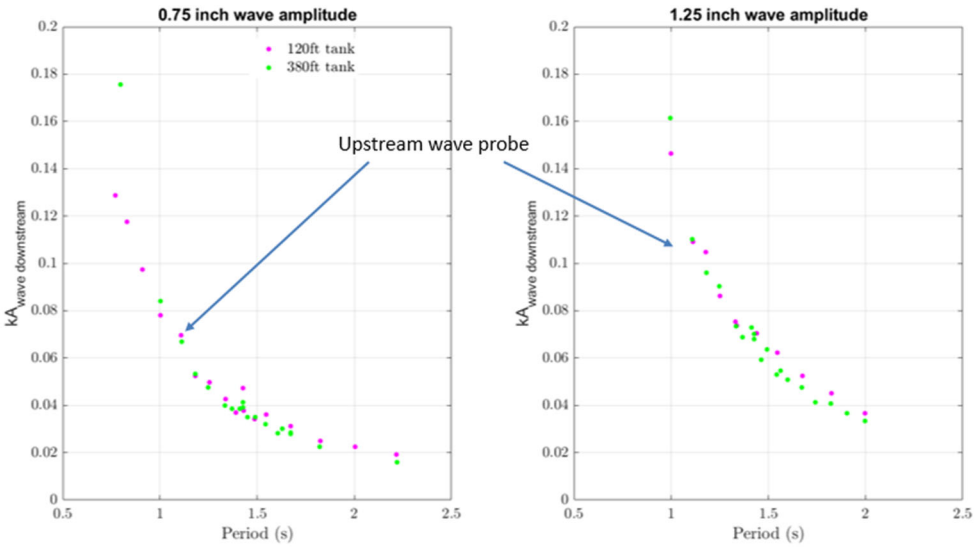

Figure 19: Local steepnesses as a function of incident wave period measured by the upstream wave probe.

The local upstream steepesses in both experiments coincide nicely for both incident wave amplitudes, which suggest that the incident waves produced by two different wavemakers (e.g. 120 and 380ft tanks) were consistent. Figure 20 shows the local downstream wave steepness data for the 2-D configuration superimposed on the previous plot.

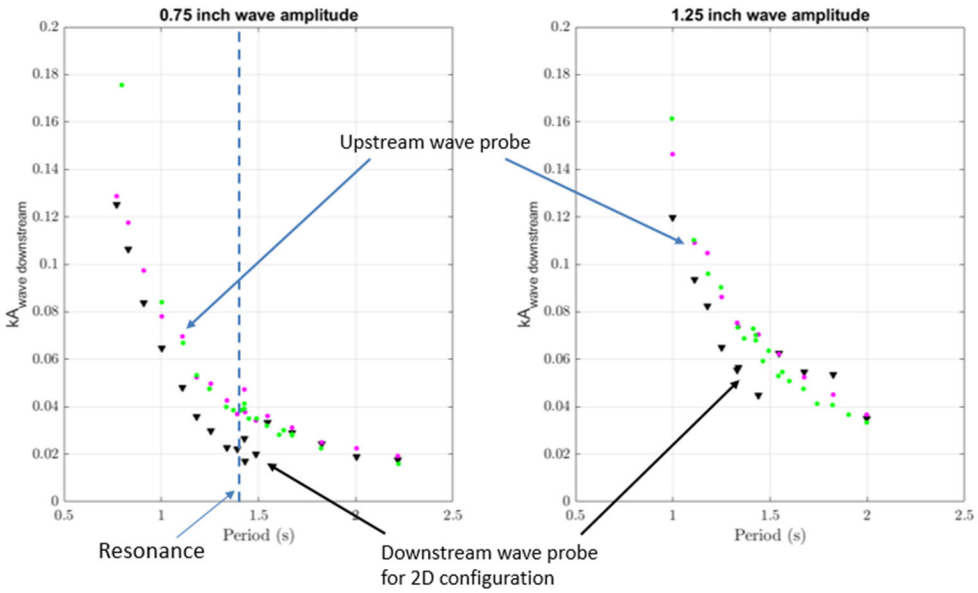

Figure 20: Local upstream and downstream (2-D) wave steepnesses as a function of incident wave period.

For short and long waves, the upstream and downstream wave steepnesses coincided with eachother. This means that these waves did not interact significantly with the cylinder, as their amplitudes remained unchanged. However, a drop-off in steepness is noticeable as resonance is approached. This indicated that the waves heavily interacted with the oscillator and caused it to absorb energy from the system. This is consistent with the results from the control volume analysis, as the largest control volume dissipation and available energy occurred at resonant conditions. Figure 21 extends this view to the 3D cylinder configuration (i.e. cylinder width in 380ft tank was much smaller than the width of the tow tank). The steepness measured by the downstream probe spikes up and becomes larger in magnitude than its upstream counterpart. This is due to the aforementioned lens-focusing effect which causes the waves to refract around the edges of the cylinder and grow in amplitude.

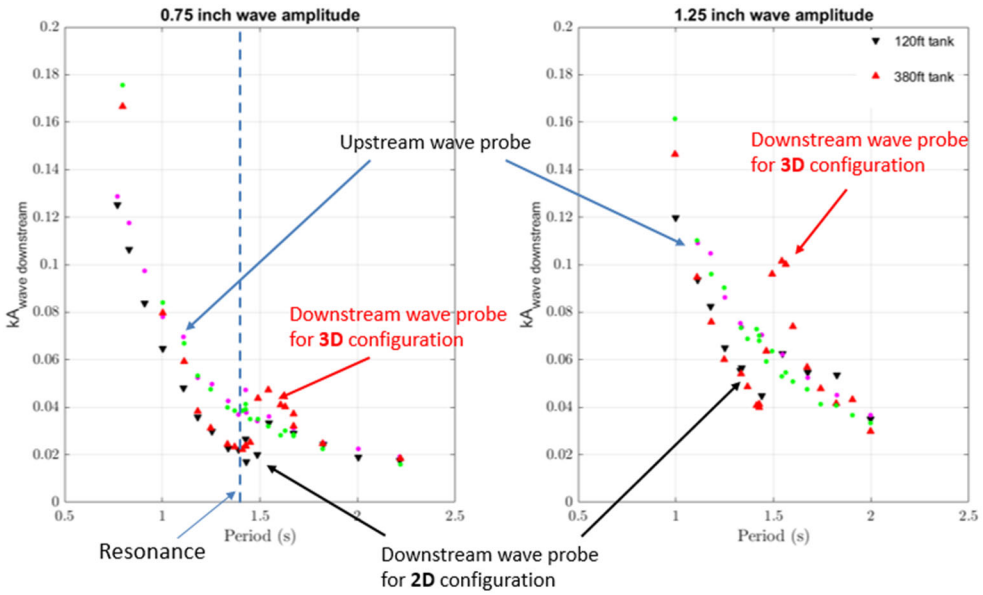

Figure 21: Local upstream and downstream (2-D and 3-D) wave steepnesses as a function of incident wave period.

These results for the undamped mechancial system showed that energy available for extraction in this WEC configuration was below the absorption efficiencies of current rotary renewable energy devices. Therefore, determining the effect on available energy of adding a second degree of freedom to the system would elucidate the viability of future implementation of an apparatus of this type.

To further explore the validity of a constant wave group speed assumption at the control volume inlet/exits utilized in the analysis described above, collaborative work with MIDN Brendan Neal, an honors student in the Weapons, Robotics, and Control Engineering major was established to work on image analysis code to allow for accurate tracking of the free surface. He developed an image processing methodology using edge-detection functions provided by MATLAB to track the free surface at each frame from a video movie of the moving cylinder. After the free surface was extracted, a polynomial was fit to match the free surface curvature. The polynomial related the y-coordinate of the free surface (in pixels) to the x-position along the frame (in pixels). The polynomial fit data was then saved for each frame, allowing for a plethora of information to be extracted. Figure 22 shows a snapshot of the image analysis output.

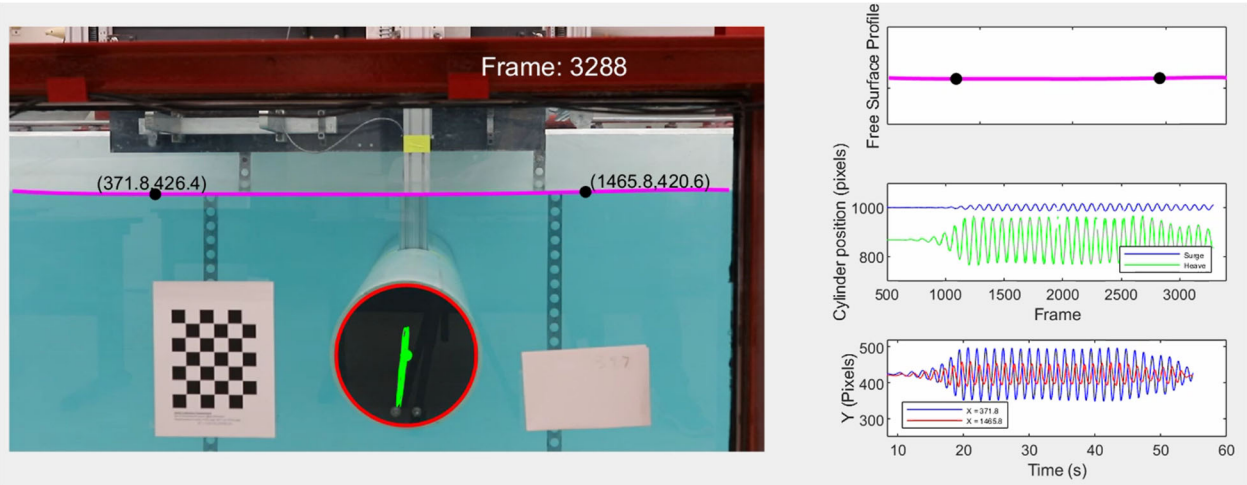

Figure 22: Output of image analysis script.

In this image, the purple line shows the polynomial fit for the free surface, the red circle indicates that the code has detected the position of the cylinder by identifying its profile, and the green dot notates the midpoint of the circle (which was used to track the surge and heave motion of the oscillator). The top plot displays the instantaneous free surface profile, the middle plot displays cylinder displacement as a function of video frame (for both axes), and the bottom plot shows the vertical position as a function of elapsed time for the points indicated on the polynomial fit. It is interesting to note that the bottom plot can be made for any point along the free surface. This means that this image analysis code provides us with an infinite amount of "virtual" wave probes.

Another wave characteristic that can be extracted through the use of image analysis was the group speed. To do this, a 3-D contour plot was made of the time history of the vertical position of each point on the free surface for a given run. The axes of the contour plot were x, y and t, and the x-t plane was isolated in order to interpolate the group speed (change in horizontal distance of a wave envelope divided by the change in time). Figure 23 shows the graphical interpolation allowing for the empirical determination of the wave group speed.

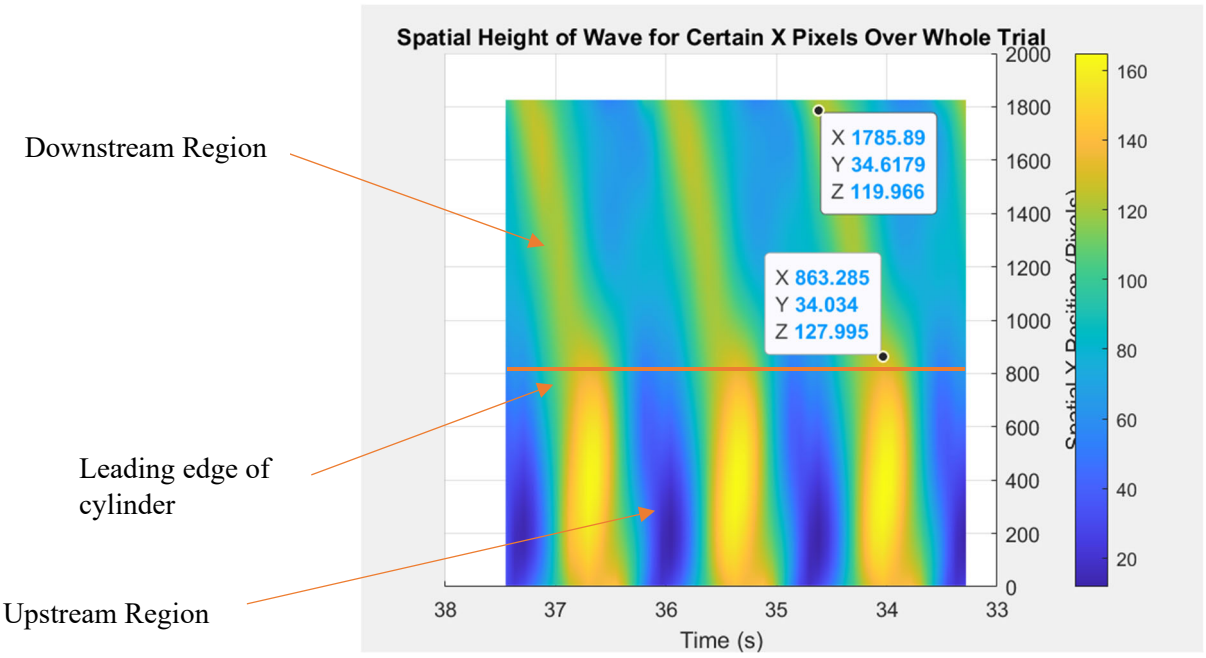

Figure 23: Interpolation of wave envelope travel for group speed determination.

The heat map depicts free surface height in pixels. The horizontal axis is elapsed time, and the vertical axis is the x-position along the free surface. One way to interpret the plot is by looking at a fixed x-position and tracking that point with time. The point oscillates between high and low vertical positions, which is consistent with the sinusoidal wave input from the wavemaker. The group speed can be visualized as the slope of the wave crest (peak). Two points were identified for use in the group speed calculation, which are notated on Figure 23. The aforementioned slope calculation was performed, and the physical dimensions of the cylinder were used as a reference for pixel to meter conversion. After this unit conversion, the group speed was calculated as 1.12 m/s, and the actual value of the group speed (calculated via traditional means) was 1.05 m/s. These two values are within 6.45% of each other, showing the viability of this technique for calculating the group speed. It is worth noting that the slope used to calculate the group speed appears after wave interaction with the cylinder. The slope is zero just upstream of the cylinder, which indicates that a standing wave is present. This means that there was a wave train present traveling in the opposite direction from the incoming incident waves. This is because the oscillating cylinder produced waves that are radiated in both the upstream and downstream directions, but this does not mean that the group speed is zero at the edges of the upstream control volume.

The next section discusses the results of the data analysis for the gantry system experiments.

B. Gantry System

Figure 24 shows the normalized instantaneous cylinder velocity, displacement and power as a function of phase angle for the gantry system (1 DOF configuration). Normalization of the

measued quantities is the same as in Figures 15 and 16. This plot shows the results over 15 wave cycles during the same experimental trial.

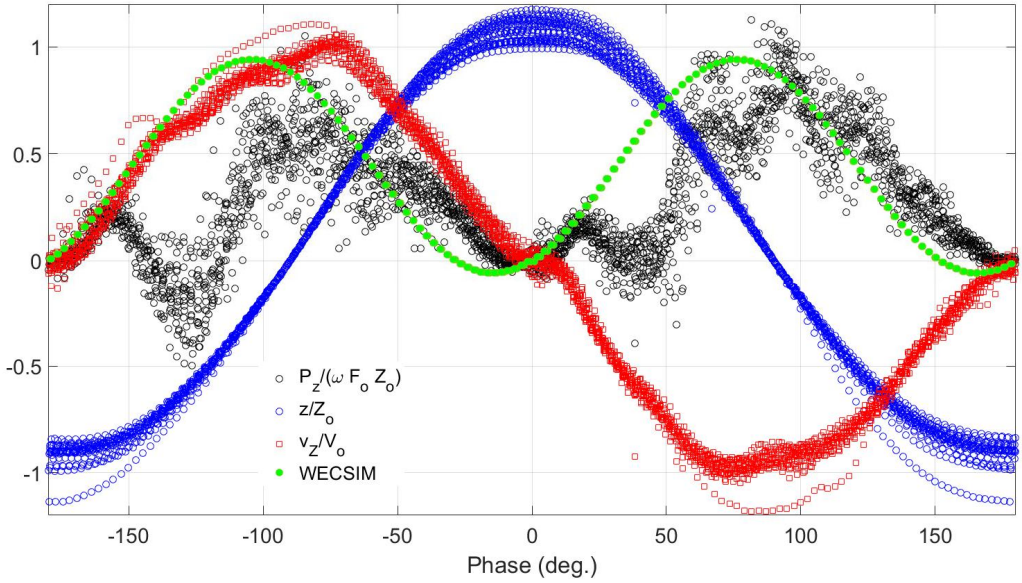

Figure 24: Normalized instantaneous cylinder position, velocity and power as a function of phase angle for gantry system (1 DOF) with $A_w = 1.0$ in, $T_w = 1.42$ s.

The shape of each curve is consistent with the corresponding curve from the mechanical undamped spring system. However, there are some significant variations in comparison with the mechanical system. It should be noted that it was not possible to remove contributions from system frictional damping from the measurements of excitation force by the load cells. Thus, hydrodynamic excitation force used to calculate available cylinder power was contaminated by unspecified frictional damping arising from the system. For example, the large dip in cylinder power at a phase angle of 125 degrees occurred while the cylinder was moving away from a maximum displacement amplitude, indicating that a parasitic frictional damping was present. Also, the disparity between experimental power and theoretical power from WECSIM increased significantly. Due to time constraints of the project, a detailed and comprehensive system identification was unable to be performed, so these are only preliminary results. The work needed to explain the observations shown in Figure 24 will be discussed in section VI.

Figure 25 shows the energy available for extraction from the WEC system at a range of incident wave periods and restoring spring constants. For all experimental trials, the magnitude of $F_{damp,cont}$ was set to zero to mimic trials done with the undamped mechanical spring system.

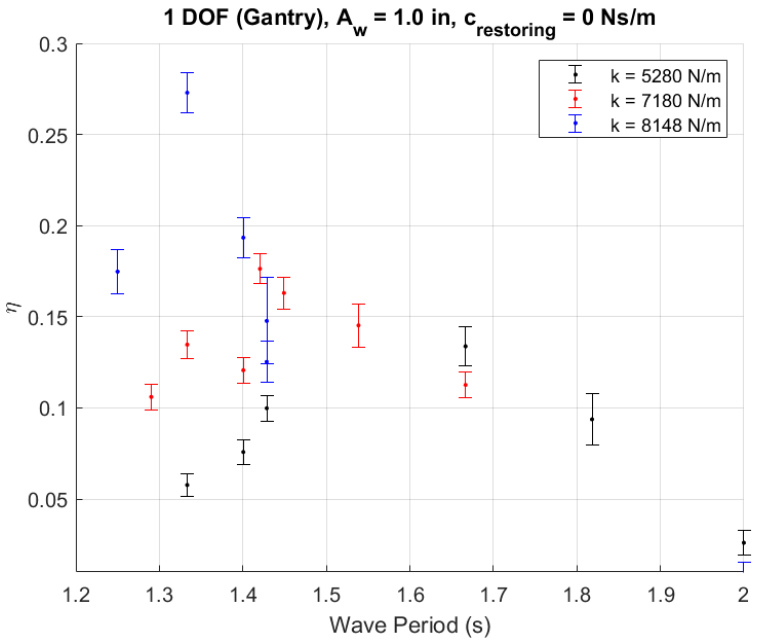

Figure 25: Energy available for extraction vs incident wave period for 3 different restoring spring constants.

The initial experiments conducted with the 1 DOF configuration on the gantry were done with a restoring spring magnitude of $k = 5.28$ kN/m to match the resonant frequency of the undamped mechanical spring system. This was done to allow for a direct comparison between the two setups. However, the peak value of available energy occurred at a wave period of 1.67s rather than 1.48s. This shift in the resonant period was partly caused by the aforementioned system friction, which created large resistance to cylinder movement. Furthermore, the shift in resonance was also a direct result of the mass of the entire system being different. With the undamped mechanical spring system, the only moving parts were the cylinder, the sting and the rollers that connected the sting to the rail. With the gantry, however, the masses of the cylinder and the sting must be added to the mass of the entire gantry arm assembly. When thinking of the system as a mass-spring-damper assembly (as discussed in section I.B), its resonant period of oscillation T can be written as:

$$\frac{2\pi}{T} = \sqrt{\frac{k_{spring,cont}}{m_{moving}+m_a}} \tag{23}$$

Where $k_{spring,cont}$ is the spring constant of the restoring spring, m_{moving} is the mass of the system that is moving during experiments and m_a is the aforementioned added mass. This equation does not consider the effects of damping. Still, it shows that when m_{moving} increases and $k_{spring,cont}$ remains the same T increases. This is reflected by the aforementioned resonant period shift.

Additionally, the magnitude of the available energy for extraction at resonance decreased by nearly 50% compared to the undamped mechanical spring system. This damped response of the gantry to the incident waves was most likely caused by the friction in the gantry. In an effort to explore this, the magnitude of the spring constant used in the system control force input was

increased to 7.18 kN/m and 8.148 kN/m, with trials done over the range of incident wave periods for each. Increasing the spring constant caused the resonant wave period to decrease (consistent with equation (23)) and the available energy for extraction at resonance to increase.

The error bars displayed for each data point in Figure 25 were generated through an uncertainty analysis [16]. The analysis focused on finding the expanded uncertainty associated with each measurement instrument and propagating it through the control volume analysis equations to the available energy calculation using equation (24):

$$U_f = \sqrt{\left(U_{x_1}\frac{\partial f}{\partial x_1}\right)^2 + \left(U_{x_2}\frac{\partial f}{\partial x_2}\right)^2 + \ldots \left(U_{x_n}\frac{\partial f}{\partial x_n}\right)^2} \quad (24)$$

Where U_f is the final calculation of uncertainty for available energy, U_{x_n} is the uncertainty associated with the n^{th} term in the calculation of available energy and $\frac{\partial f}{\partial x_n}$ is the partial derivative of available energy with respect to the n^{th} term in its calculation (otherwise known as the "sensitivity of f with respect to x_n").

Two main sources of uncertainty were considered for each measurement device: linearity of the calibration fit and random error. Prior to experimental use, each device was loaded up incrementally to a maximum value with the voltage output of the device recorded at each load. The data was fitted through a least-square-error linear regression to obtain a calibration constant, which was used to convert the raw voltage output of the devices to useful units for analysis. The strength of the calibration fit determined how accurate the experimental data was, so the standard deviation of the residuals at each data point were factored into the uncertainty calculation for each instrument using the student-t statistic. The random error of each device was determined by recording 10s of data in still conditions prior to each trial. The data set for each instrument was broken into 100 subintervals and the mean of each subinterval was calculated. Then, the standard deviation of the calculated means was also factored into the uncertainty calculation for each instrument using the student-t statistic. The final source of error was the uncertainty associated with the model of applied gantry forces, which was an ideal case and likely did not perfectly match the force applied by the motors at the end effector during experiments. These ideal gantry forces were subtracted from the load cell readings during the control volume analysis. This was accounted for by offsetting the uncertainty of each available energy calculation by 0.005. This is our initial estimate as full and comprehensive system identification has not been completed as of yet. All uncertainties were quoted at 95% confidence.

Figure 26 shows the energy available for extraction from the WEC system operating in a 2 DOF configuration.

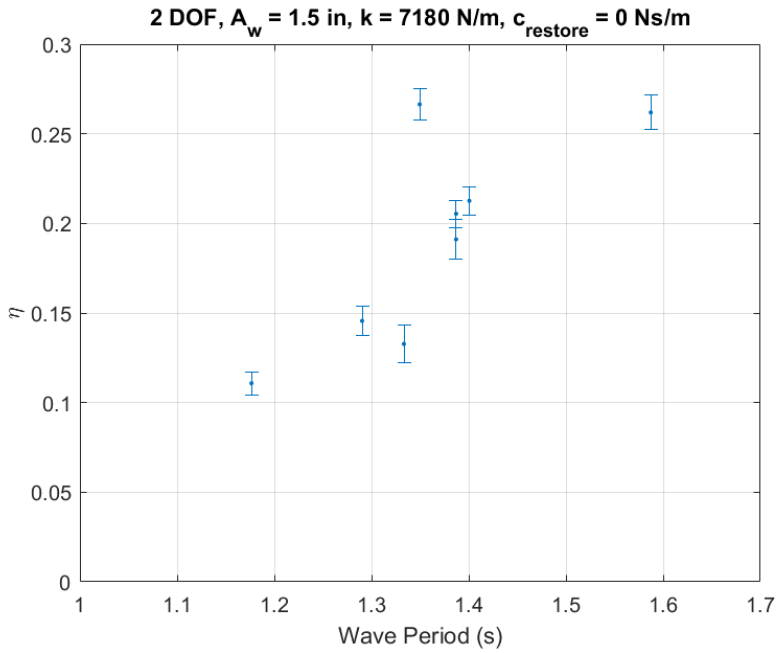

Figure 26: Energy available for extraction vs incident wave period.

For the 2 DOF experimental trials, the incident wave amplitude was increased to 1.5 in to provide the system with enough energy to overcome friction and allow for movement in both axes. Figure 25 and 26 both show that the frictional damping in the system caused the WEC response to the incident waves to be overdamped. As discussed previously, the hydrodynamic force acting on the cylinder could not be isolated due to this friction, and therefore a direct comparison between the available energy results of the undamped mechanical spring system and the gantry could not be made. However, when comparing the 1 DOF and 2 DOF gantry results to each other for $k = 7.180$ kN/m it is clear that adding a second degree of freedom to the system increased the energy available for extraction by around a factor of two. The error bars displayed in Figure 26 were found using the same method as with the 1 DOF gantry experiments discussed above.

A dissipated energy analysis was not performed for any of the gantry setup experiments. The combination of radiation waves produced by the oscillating cylinder and small cylinder displacements led to the wave probe data being inconclusive.

To track the free surface of the water in the 380ft tank, Laser Induced Fluorescence (LIF) [11,12] was used. To use this technique, Fluorescein sodium salt, which is a fluorescent dye, was added to the water around the cylinder and a 5W continuous laser was fixed to the tow tank carriage. The laser emitted a sheet of light that illuminated the dye and allowed for the change in elevation of the free surface as a function of time to be tracked via camera. The cameras had a resolution of (1920x1080 pixels^2) each and tracked the free surface at a frame rate of around 1890 fps. From this free surface tracking, important wave characteristics such as amplitude, period, phase speed, etc. were able to be extracted. The amount of incident wave that was tracked using LIF corresponds to around 2m upstream and downstream of the cylinder. The cameras were mounted onto the tow carriage at a 5-degree angle from the horizontal in order to capture as

much of the free surface as possible. Figure 27 shows the installation of the 5W laser onto the tow tank carriage.

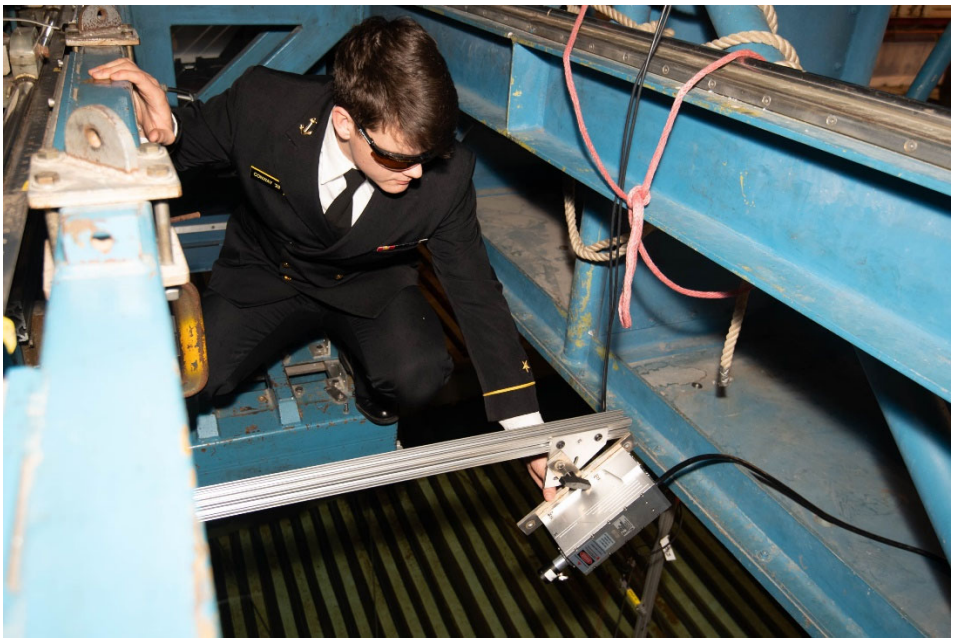

Figure 27: 5W laser being installed onto the 380ft tank Low Speed Carriage.

The laser setup configuration allowed for fine adjustment of laser pitch angle and position relative to the cylinder. Figure 28 shows the results of the camera vision analysis performed on the recorded footage.

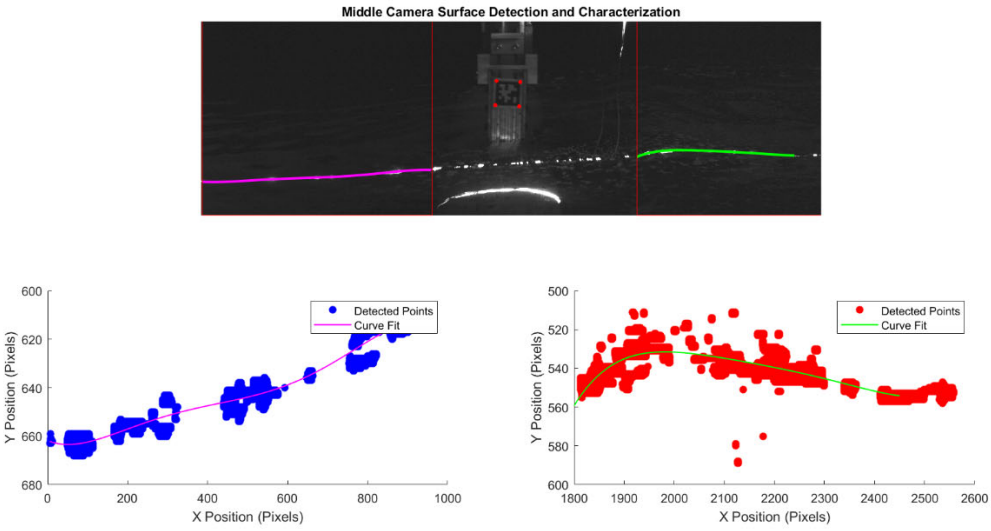

Figure 28: Middle camera surface characterization.

This analysis was also done with the help of MIDN Brendan Neal. Figure 28 shows the illuminated pixels generated by the LIF technique and the polynomial curves used to fit the pixel data. These curves are a mathematical representation of the free surface and allow for useful

wave characteristics, like group speed, to be calculated. The next step will be to use camera calibration images to convert from pixel units to physical length units, which will make calculating wave characteristics possible.

V. Conclusions

For the mechanical spring setup (1 DOF), the highest available energy for extraction was 35% and occurred at the resonant period of 1.48s. The total energy dissipated in the control volume at this incident period was 90%. The energy budget was qualitatively balanced at low and high wave periods, but at and around resonance there was a much larger disparity between the energy available for extraction and total energy dissipated within the control volume. This indicates that the 1 DOF configuration left a lot of energy unavailable for harvesting. Additionally, with larger incident wave amplitudes at periods beyond the resonant period the assumption of a constant wave group speed throughout the control volume appears to break down.

For the gantry setup, large amounts of system friction caused the cylinder response to be overdamped in both the 1 DOF and 2 DOF configurations. This friction made it impossible for the hydrodynamic force on the cylinder to be isolated, making comparisons between available energy results from the undamped mechanical spring system and gantry system meaningless. Additionally, the extra moving mass of the gantry in comparison to the mechanical spring apparatus caused the resonant period of the system to shift from 1.48s to 1.67s (with k remaining constant), further complicating the comparison between system setups. However, when comparing the results of the 1 DOF and 2 DOF gantry experiments it is clear that adding an additional degree of freedom increased the energy available for extraction from the system by a factor of two.

VI. Future Work

Future work on this project will include a detailed and comprehensive system identification. This will consist of characterizing the friction present in the gantry in order to properly account for it in the system control software. Also, free decay tests will be performed on the cylinder to allow for calculation of nonlinear viscous damping coefficients. This will improve understanding of the viscous damping experienced by the cylinder. Once this is complete, the gantry experiments will be repeated (with zero restoring damping force) and the control volume analysis will be repeated with the hydrodynamic force properly isolated. This will allow for comparison to the undamped mechanical spring system. Additionally, future experiments will include restoring damping forces calculated using equation (14) to maximize available energy for extraction. Also, the design and implementation of a power takeoff damper will be critical in determining how much useful energy can be extracted from this oscillating WEC.

VII. References

[1] OpenEI, "Wave Energy," 2015. [Online].

[2] A. Babarit and G. Delhommeau, "Theoretical and numerical aspects of the open source BEM solver NEMOH,"in Proceedings of the 11th European Wave and Tidal Energy Conference (EWTEC2015), Nantes, France, 2015.

[3] Dean, Dalrymple. "Water Wave Mechanics for Engineers and Scientists," 2nd ed. Singapore: World Scientific Publishing Co. Pte. Ltd., 1991.

[4] P. Webb, "Introduction to Oceanography," Roger Williams University, 2019. [Online]

[5] S. James, R. Stull, "Breaking Waves," UBC ASTC 113, 2019. [Online]

[6] A. Khait, L. Shemer, "On the kinematic criterion for the inception of breaking in surface gravity waves: Fully nonlinear numerical simulations and experimental verification," Physic of Fluids 30, 057103 (2018); https://doi.org/10.1063/1.5026394.

[7] B. R. Munson, T. H. Okiishi, W. W. Huebsch, and A. P. Rothmayer, Fundamentals of Fluid Mechanics, 4th ed. Hoboken, NJ: John Wiley and Sons, Inc., 2002.

[8] K. Reichl, K. Hourigan, and M. C. Thompson, "Flow past a cylinder close to a free surface," Journal of Fluid Mechanics, vol. 533, pp. 269–296, 2005.

[9] J. Sheridan, J. Lin, and D. Rockwell, "Flow past a cylinder close to a free surface," *Journal of Fluid Mechanics*, vol. 330, pp. 1–30, 1997.

[10] D. Evans, "A theory for wave power absorption by oscillating bodies," Journal of Fluid Mechanics, vol. 77, pp. 1–25, 1976.

[11] X. Liu and J. Duncan, "An experimental study of surfactant effects on spilling breakers," Journal of Fluid Mechanics, vol. 567, pp. 433–455, 2006.

[12] A. Charogiannis, J. S. An, and C. N. Markides, "A simultaneous planar laser-induced fluorescence, particle image velocimetry and particle tracking velocimetry technique for the investigation of thin liquid-film flows," Experimental Thermal and Fluid Science, vol. 68, pp. 516–536, 2015. [Online].

[13] McCormick. "Ocean Wave Energy Conversion," John Wiley & Sons Inc., 1981

[14] Luksa Luznik, Karen A. Flack, Ethan E. Lust, Katharin Taylor, "The effect of surface waves on the performance characteristics of a model tidal turbine", Renewable Energy Volume 58, October 2013, Pages 108-114

[15] Y.-H. Yu, M. Lawson, K. Ruehl, and C. Michelen, "Development and Demonstration of the WEC-Sim Wave Energy Converter Simulation Tool," in Proceedings of the 2nd Marine Energy Technology Symposium, METS 2014, Seattle, WA, 2014.

[16] Ratcliffe, C. and Ratcliffe, B. " Doubt-Free Uncertainty in Measurements", Springer, 2015.